Geophysical Research Letters

RESEARCH LETTER
10.1029/2021GL094903

Geological Characteristics and Targets of High Scientific Interest in the Zhurong Landing Region on Mars

Jiannan Zhao[1,2], Zijun Xiao[1], Jun Huang[1,3], James W. Head[4], Jiang Wang[1], Yutong Shi[1], Bo Wu[5], and Le Wang[1]

[1]State Key Laboratory of Geological Processes and Mineral Resources, School of Earth Sciences, Planetary Science Institute, China University of Geosciences, Wuhan, China, [2]Key Laboratory of Geological Survey and Evaluation of Ministry of Education, China University of Geosciences, Wuhan, China, [3]Chinese Academy of Sciences Center for Excellence in Comparative Planetology, Hefei, China, [4]Department of Earth, Environmental and Planetary Sciences, Brown University, Providence, RI, USA, [5]Department of Land Surveying and Geo-Informatics, Planetary Remote Sensing Laboratory, The Hong Kong Polytechnic University, Hong Kong, China

Abstract We used imaging, laser altimeter and thermal infrared data to map a 0.5 by 0.5° area containing the landing site of the Zhurong rover of the Tianwen-1 mission. We analyzed the regional topography and thermophysical characteristics, and identified and characterized cones, impact craters, polygonal troughs, ridges and aeolian bedforms. An absolute model age of 757 ± 66 Ma was obtained for the major unit dominating the study area, younger than previous geological mapping results. We propose several targets of high scientific interest for Zhurong and a stratigraphic model composed of five layers (from bottom to top: Noachian basement, Early Hesperian volcanic ridged plains, Vastitas Borealis Formation materials, rocky materials and loose materials). The geomorphic features identified, the proposed stratigraphy and the regional geological evolution scenario set the stage for the Zhurong rover to continue to carry out its exploration of Mars.

Plain Language Summary Tianwen-1 is China's first independent Mars mission. It consists of an orbiter and a lander and a rover (Zhurong). The Zhurong rover successfully touched down on the surface of Mars on May 15, 2021. The landing site lies in southern Utopia Planitia, in the northern lowlands of Mars. We identified various geomorphologic features within an area of 0.5 by 0.5° centered around the landing site of the Zhurong rover using image, elevation and temperature remote sensing data. We propose a history and geological evolution of the region to set the stage for the Zhurong rover exploration and analysis.

Jiannan Zhao and Zijun Xiao contributed equally to this work.

Key Points:

- We conducted detailed geological mapping of the Zhurong landing region on Mars
- High scientific interest targets for Zhurong rover including cones, pitted-wall craters, aeolian bedforms, polygons, and ridges are proposed
- A middle Amazonian surface age is suggested and a five-layer stratigraphic model of the Zhurong landing region is proposed

Supporting Information:

Supporting Information may be found in the online version of this article.

Correspondence to:

J. Huang,
junhuang@cug.edu.cn

Citation:

Zhao, J., Xiao, Z., Huang, J., Head, J. W., Wang, J., Shi, Y., et al. (2021). Geological characteristics and targets of high scientific interest in the Zhurong landing region on Mars. *Geophysical Research Letters*, *48*, e2021GL094903. https://doi.org/10.1029/2021GL094903

Received 25 JUN 2021
Accepted 4 OCT 2021

1. Introduction

China's planetary exploration missions are officially named Tianwen ("questions to heaven" in Chinese). Tianwen-1 is the first Mars mission of China, which consists of an orbiter and a lander/rover composite (Wan et al., 2020). The orbiter was captured by Mars with a large elliptical orbit (a perigee of 280 km and an apogee of 59,000 km) on February 10, 2021. The orbiter is equipped with seven scientific instruments (Tan et al., 2021; Ye et al., 2017): Moderate Resolution Imaging Camera (MoRIC: 100 m/pix @ 400 km), High Resolution Imaging Camera (HiRIC: 2 m/pix @ 400 km), Mars Mineralogical Spectrometer (MMS: 2.8 km/pix @ 265 km), Mars Orbiter Magnetometer (MOMAG), Mars Orbiter Scientific Investigation Radar (MOSIR), Mars Ion and Neutral Particle Analyzer (MINPA) and Mars Energetic Particles Analyzer (MEPA).

The lander and rover safely landed in southern Utopia Planitia after a 3-month orbital mapping of the candidate landing region (B. Wu et al., 2021; X. Wu et al., 2021). The rover is named Zhurong (the God of fire in Chinese mythology). The scientific objectives of the rover include investigation of the surface composition, regolith characteristics, water-ice distribution, magnetic field, and environment at the surface (Jia et al., 2018). Zhurong is equipped with six scientific instruments (Tan et al., 2021; Ye et al., 2017): (a) Mars Surface Composition Detector (MarSCoDe), which consists of an elemental chemistry component using a Laser Induced Breakdown Spectrometer (LIBS: Si, Al, Fe, Mg, Ca, Na, O, C, H, Mn, Ti, S) and a mineralogy detection component using a Visible and Near Infrared Spectrometer (VNIS: 850–2400 nm); (b) Multispectral Camera (MSCam: 470–1025 nm) with 8 bands at 480, 525, 650, 700, 800, 900, 950, and 1,000 nm; (c)

Mars Rover Penetrating Radar (RoPeR: 35–75 MHz and 800–1800 MHz); (d) Mars Rover Magnetometer (RoMAG), the detection range is ±65,000 nT with 0.01 nT resolution; (e) Mars Climate Station (MCS), measuring near-surface atmospheric temperature and pressure and wind speed and direction; and (f) Navigation and Topography Camera (NaTeCam).

In order to investigate the geological context of the landing area and propose targets of high scientific interest for the Zhurong rover and related analyses, we mapped a 0.5-degree by 0.5-degree region centered at 25.1°N, 109.9°E, and proposed a stratigraphic and evolutionary scenario for the region.

1.1. Data and Methods

We used Mars Orbiter Laser Altimeter (MOLA; Smith et al., 2001) Mission Experiment Gridded Data Record (MEGDR: 128 ppd) to visualize the regional topography and the Precision Experiment Data Record (PEDR) to extract topographic profiles. The Thermal Emission Imaging System (THEMIS; Christensen et al., 2004) global mosaic (~100 m/pixel; Edwards et al., 2011) provided regional geomorphological context and qualitative assessment of the thermophysical properties of the surface materials. Thermal inertia derived from THEMIS nighttime infrared (IR) data (Fergason et al., 2006) provided insights into the effective particle size (Presley & Christensen, 1997) of the surficial materials with the assumption that the materials are unconsolidated. We used the Context Camera (CTX; Malin et al., 2007) global mosaic (~6 m/pixel; Dickson et al., 2018) and images from the High Resolution Imaging Science Experiment (HiRISE, ~25–30 cm/pixel; McEwen et al., 2007) to characterize the detailed geomorphologic features. We carried out impact crater size-frequency distribution (CSFD) measurements (Michael & Neukum, 2010) on the CTX global mosaic with ArcGIS plugin Cratertools (Kneissl et al., 2011) and analyzed the CSFD data with Craterstats2 (Michael & Neukum, 2010).

2. Results

2.1. Regional Topography and Thermal Physical Properties of the Study Area

The landing area is located in the southern part of Utopia Planitia, and north of the dichotomy boundary (Figure 1a), which is the area separating southern Noachian highlands and younger northern lowlands. The Elysium volcanic province lies to the east of the landing area, while the Isidis basin lies to the southwest. The study area is within a geological unit previously mapped as the Late Hesperian lowland unit (lHl; Tanaka et al., 2014). This unit is mainly composed of the Vastitas Borealis Formation (VBF) materials and occurs continuously across most of the northern plains. The VBF has been interpreted as sediments of fluvial, lacustrine, or marine in origin (Kreslavsky & Head, 2002; Tanaka, 2005).

The study area has a higher topography in the south (Figure 1b), likely due to the regional slope of Utopia basin from its circular margin toward the interior. The elevation range in the study area is about 200 m, while the northward slope is ~0.25° (30-km baseline). The nearest cone and largest impact crater are ~6.8 and ~13.5 km away from the landing site, respectively.

The average TES (Thermal Emission Spectrometer; Christensen et al., 2001) bolometric albedo of the mapping area is 0.234, with a standard deviation of 0.001 and the average DCI (Dust Cover Index; Ruff & Christensen, 2002) is 0.941 with a standard deviation 0.011. Both the albedo and DCI indicate that the surface of the study area is relatively dusty at TES spatial resolution (~3 km by ~5 km). THEMIS nighttime IR is a good proxy for thermal inertia, and we observed thermal inertia variation within the study area (Figure 1c). A larger effective particle size is indicated by warmer colors while a smaller effective particle size corresponds to cooler colors. Ejecta of impact craters show elevated thermal inertia; we named these as rocky ejecta craters (REC). Lower thermal inertia areas correspond to cones and some troughs which contain aeolian bedforms. An area of 600 m by 600 m centered at the landing site (the approximate activity area of Zhurong rover in the 3-month primary mission) has a thermal inertia of 321–376 $JK^{-1}\ m^{-2}\ s^{-1/2}$ with a standard deviation of ~12 $JK^{-1}\ m^{-2}\ s^{-1/2}$. The thermal inertia of the study area corresponds to an effective particle size larger than 1 mm (Presley & Christensen, 1997), assuming the surface materials are unconsolidated. Considering a 20% error in the thermal inertia calculation (Fergason et al., 2006), the lower limit of thermal inertia is ~257 $JK^{-1}m^{-2}s^{-1/2}$, which corresponds to an effective particle size of ~580 μm for

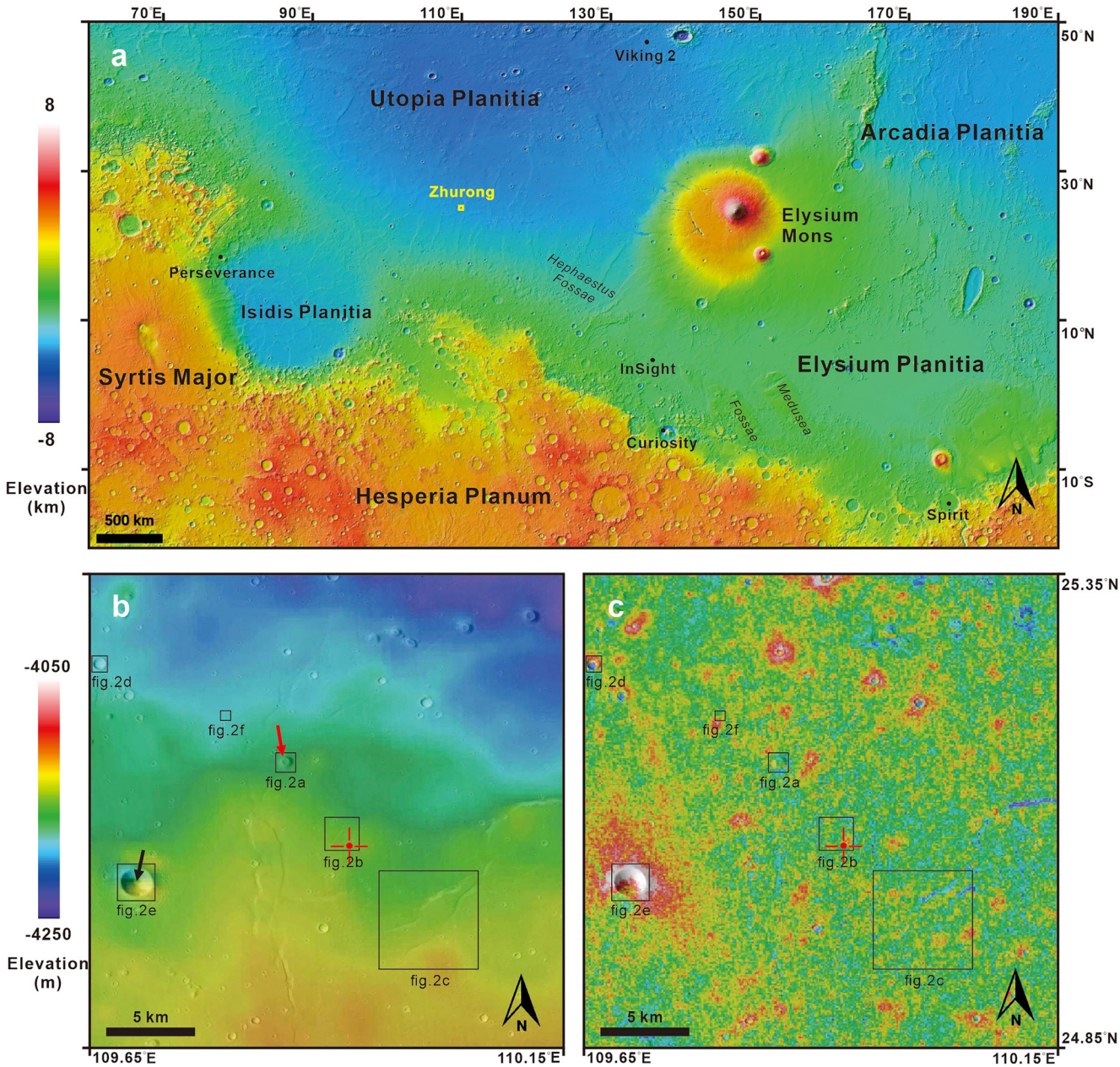

Figure 1. (a) Color-coded MOLA MEGDR topographic context. The study area is outlined with a yellow square, which corresponds to the location of (b) and (c). The landing sites of Viking 2, Spirit, Curiosity, InSight, and Perseverance are shown as black dots. (b) Color-coded MOLA MEGDR over the context camera (CTX) global mosaic. The southern portion of the study area is higher than the north. The red cross indicates the landing site of Zhurong [same in (c)]. The nearest cone is labeled as A (the red arrow), and the largest impact crater as B (the black arrow). (c) Color-coded THEMIS nighttime IR global mosaic (a good proxy of thermal inertia) over the CTX global mosaic. Warm color areas are ejecta of craters with elevated thermal inertia, and cold color areas are locations of cones and polygons with lower thermal inertia. The cross symbol indicates the location of the landing site.

the unconsolidated materials. We calculated the diurnal surface temperature with the KRC model (Kieffer, 2013) on Mar 15, June 15, July 15, and August 15 (Figure S1), which correspond to the dates at 1-month interval of the primary mission of the Zhurong rover. The maximum temperature is ~269 K at 13:00 p.m local time, and the minimum temperature is ~186 K at 5:30 a.m local time.

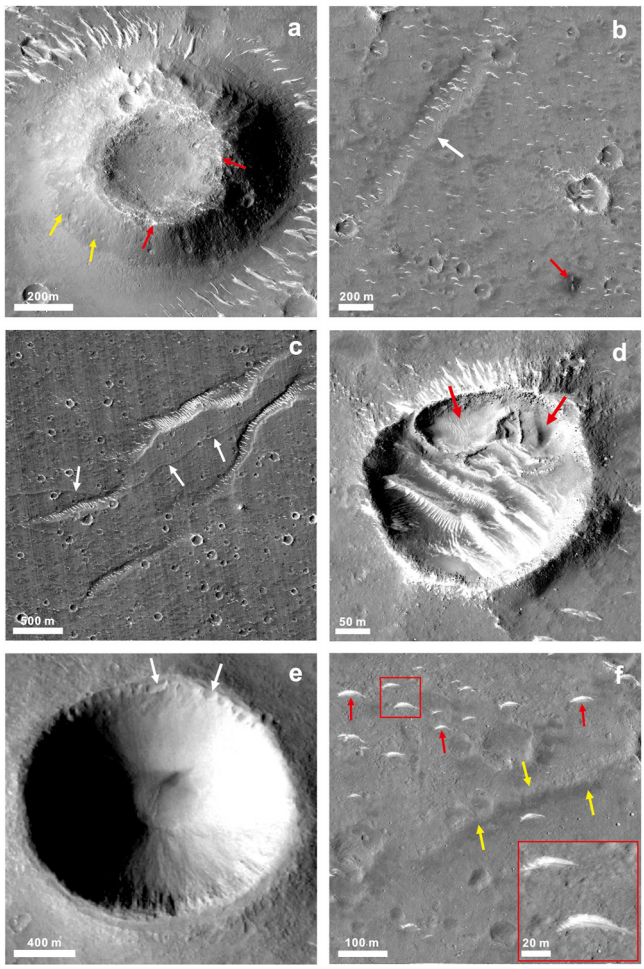

Figure 2. Geomorphic features in the landing region. The locations of (a–f) are labeled in Figures 1b and 1c. (a) The nearest cone structure from the landing site (centered at 25.16°N, 109.86°E) is labeled "A". It is ~40 m in height with a basal diameter of ~1,156 m. The circular summit crater has a diameter of ~532 m. Relatively high albedo materials are exposed on the rim of the summit crater (red arrows). Relatively dark materials occur on the upper flank of the cone (yellow arrows). Aeolian bedforms are distributed radially around the cone. HiRISE ID: ESP_069876_2055. (b) The nearest trough is filled with bedforms (the white arrow; centered at 25.08°N, 109.92°E). It has a length of ~1.1 km and a width of ~0.15 km. HiRISE ID: ESP_069665_2055. The Tianwen-1 lander and the Zhurong rover are indicated by the red arrow. (c) The longest ridge in the study area is labeled with white arrows and centered at 24.99°N, 110.02°E. It is about 5.6 km long and the width ranges from ~40 m to more than 100 m. It intersects a polygonal trough that is about 300 m wide. CTX global mosaic. (d) An impact crater with equator-facing and raised-rim pits is indicated by red arrows (central coordinates: 25.04°N, 109.91°E). HiRISE ID: ESP_069665_2055. (e) The largest impact crater ("B") in the study area (centered at 25.03°N, 109.70°E) has a diameter of ~1900 m and a depth of ~300 m. Equator-facing and raised-rim pits (white arrows) are identified on the uppermost part of the crater wall. Relatively dark-toned materials occur on the floor. CTX global mosaic. (f) An example of a relatively straight ridge (yellow arrows) and barchan-shaped aeolian bedforms (red arrows) on the inter-crater terrain is centered at 25.21°N, 109.80°E. HiRISE ID: ESP_069876_2055.

2.2. Geomorphic Features

2.2.1. Cones

Over 10 cones occur in the study area and most of them are characterized by circular summit craters. We identified both eroded summit craters and elongated/coalesced shapes (Table S1). Relatively lighter-toned materials are exposed on the rim of the summit crater, and relatively darker-toned materials are present on the upper flank (Figure 2a). We observed aeolian bedforms characterized by a relatively bright tone surrounding this cone in a generally radial pattern.

2.2.2. Polygonal Troughs

Tens of giant troughs have been identified in the area. The length of the troughs varies from ~1.1 to ~8 km, and the width range is ~0.1–~1 km. Trough depths vary between ~6 and ~60 m, with an average of ~24 m. These troughs belong to the polygonal trough system in the southern Utopian Planitia (Ivanov et al., 2014). The nearest polygonal trough is ~1.2 km away from Zhurong's landing site (Figure 2b). The trough is oriented in a NE-SW direction. Parallel aeolian bedforms occur in the trough with crest lines oriented perpendicular it.

2.2.3. Ridges

We have mapped tens of ridges in the study area, and the length varies between ~0.4 and ~5.6 km. These ridges usually have rounded crests and relatively symmetrical cross-sectional profiles, which is distinctly different from wrinkle ridges often seen on volcanic plains. The ridges can be further divided into two types: Type 1 is widely distributed in the study region and is relatively short and straight (Figure 2f), while Type 2 is rare and usually longer and more sinuous (Figure 2c). The longest ridge in the study region is shown in Figure 2c.

2.2.4. Impact Craters

We have identified 436 impact craters, in which 12 craters have diameters larger than 500 m and the rest are between 200–500 m in diameter. Rocky ejecta craters (RECs) have been identified throughout the study area, characterized by elevated nighttime temperature in the THEMIS nighttime mosaic (Figure 1c). The rim crests of RECs usually appear sharp. The minimum diameter of REC-type craters is 10 m. There is a ghost crater of ~10 km diameter centered at 25.12°N, 109.97°E and previously identified by Ivanov et al. (2014).

Interestingly, there are 40 craters with raised-rim pits on their equator-facing wall. The pits occurred on the upper portion of the walls in chains or clusters (Figure 2d). These pits are unlikely to have formed by collapse but may be due to the energetic release of volatiles (Orgel et al., 2019) or the sublimation of an ice-rich layer near the surface. The minimum diameter of the pitted-wall craters is ~200 m.

The largest impact crater (B) displays a concentric ejecta blanket. Raised-rim pits occur on the uppermost part of the equator-facing crater wall. Relatively dark-toned materials occur on the floor of the crater (Figure 2e).

2.2.5. Aeolian Features

Extensive light-toned aeolian sediments occur within the craters, polygonal troughs, around the cones and on the terrain between the features

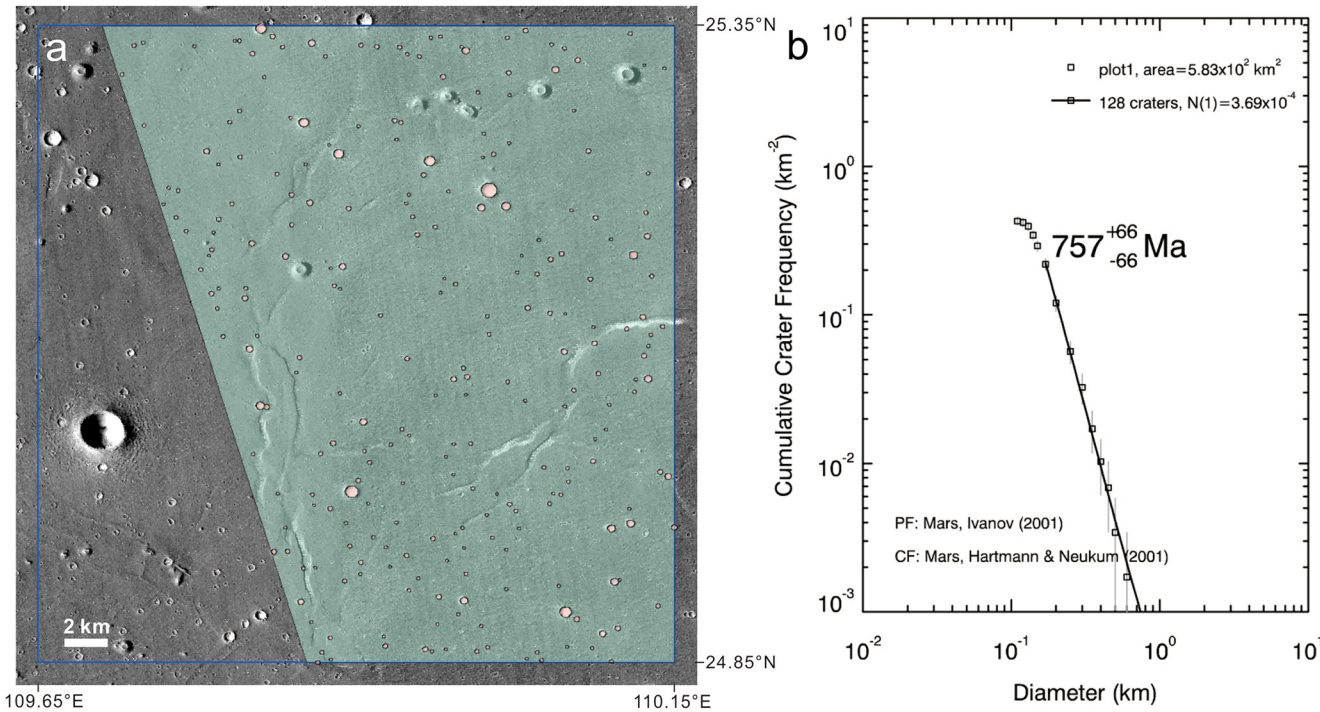

Figure 3. Crater counting region (a; the area with light green color) and cumulative crater size-frequency distribution for the study area (b). The background of (a) is context camera (CTX) mosaics.

described above (Figure 2f). Most of the aeolian sediments formed granule ripples (Sharp, 1963; Zimbelman, 2010), as well as some complex dunes, such as star dunes and feathery dunes in craters (Figure 2d). These granule ripples are characterized by low height, straight crest, and symmetric slopes. Some of them are similar to barchan-shaped dunes with asymmetric slopes (Figure 2f). The bedforms are tens to hundreds of meters in length. The main directions of the bedforms are NW-SE and E-W. However, the orientation of bedforms that occur in low regions (e.g., troughs and craters) and around cones is controlled by the local topography.

2.2.6. Absolute Model Age

The study region has a relatively uniform surface texture, with no evidence for distinctive subunits, so we consider it as a single terrain unit for the purpose of crater size-frequency distribution measurements. To better constrain the age of the landing region, we performed impact crater size-frequency distribution measurements in the study region. Because the western part of the region is heavily affected by secondary craters and ejecta of crater B, we conducted crater counting in the central and eastern parts of the study region, with a total area of about 583 km^2 (Figure 3a). In addition, we excluded crater clusters and irregular craters to further decrease the influence of secondary craters. The result shows that the estimated absolute model age of the region is 757 $\pm$ 66 Ma (Figure 3b), which is much younger than the ~3.6–3.5 Ga absolute model age of the VBF unit obtained by Ivanov et al. (2014) and the late Hesperian age estimated by Tanaka et al. (2014). This discrepancy is due to the fact that previous age determinations are conducted over larger areas, and the ages are obtained with craters of much larger sizes (larger than 1 km). However, some local resurfacing processes (e.g., thin lava flows) may not affect the large craters with elevated rims while small craters may have been totally buried. In our study region, most of the craters are less than 1 km except crater B. Therefore, we interpret our dating result to represent a local emplacement/resurfacing event/process that occurred in the study area in the Middle Amazonian. In addition, to compare with previous dating results, we dated a larger area (2 × 2° region centered on the landing site) with craters larger than 1 km (Figure S2). An absolute model age of ~3.23 (+0.15/−0.47) Ga was acquired, which is consistent with the Late Hesperian age reported by Tanaka et al. (2014) and represents the age of VBF unit.

3. Discussion

3.1. Targets for the Zhurong Rover

3.1.1. Cone A

There are three possible origins for cone A: a cinder cone (Brož et al., 2017), a volcanic rootless construct (Hamilton et al., 2011) and a mud volcano (Ivanov et al., 2014; Komatsu et al., 2016; Skinner & Tanaka, 2007). It is difficult to rule out any of these possibilities with only orbital geomorphological measurements (Brož & Hauber, 2012). Zhurong rover exploration of cone A will be the first high-resolution, in situ analysis of these widespread and enigmatic features. The RoPeR instrument onboard Zhurong rover could detect potential evidence of materials (lava or mud) and their transportation conduits, which can rule out the origin as rootless cones. The in-situ mineralogy and elemental measurements by Zhurong rover's MarSCoDe could determine the existence and percentage of hydrated minerals, which would provide insights into distinguishing between lava and mud origins.

If the origin of cone A is a cinder cone or a rootless cone, the composition of the volcanic materials will provide important information on Amazonian volcanism from the first in-situ measurement. Most Amazonian volcanic materials are covered by air fall dust (Ruff & Christensen, 2002), which has hindered systematic mineralogical analysis with orbital spectra. Lava composition is thought to be similar to terrestrial basalts on the basis of geomorphology (Pasckert et al., 2012). Stockstill-Cahill et al. (2008) used thermal infrared data to describe the mineralogy of relatively dust-free window regions within Amazonis Planitia and found elevated mafic compositions implying mafic to ultramafic composition of the lava. However, Gamma Ray Spectrometer data suggest a SiO_2 percentage greater than 45 wt% in Amazonis Planitia (Newsom et al., 2007), indicating that ultramafic magmas are not likely to dominate spatially. It is critical to obtain in-situ mineral and elemental composition measurements for Amazonian volcanic materials, which can provide information about the interior of Mars and potentially the percentage of partial melting and depth of magma sources.

If cone A is a mud volcano (Ivanov et al., 2014; Komatsu et al., 2016; Oehler & Allen, 2010), the compositional measurements will provide insights into the underlying Vastitas Borealis sediments, which will be critical to test the Hesperian Ocean hypothesis (Parker et al., 1989, 1993).

3.1.2. Pitted-Wall Craters

The closest recognizable pitted-wall crater (Figure 2b) is ~0.5 km away from the landing site. The raised rim of the pits appears very fresh, which suggests a relatively young age of formation. These pits are likely to have formed from either the energetic release of volatiles (Orgel et al., 2019), or sublimation of ice in the near-surface, although the detailed mechanism is not clear. Exploration and analysis by the Zhurong rover could provide detailed geomorphic observations of the raised rim and the materials inside/outside the pits to distinguish between an explosion or collapse origin. The onboard RoPeR could detect the subsurface structure of the rim area and the north-facing crater rim, which could provide insights into the subsurface water-ice/CO_2 ice distribution. It could also provide information on any volatile discharge and release.

3.1.3. Aeolian Bedforms

Young aeolian landforms can reveal the direction of the recent prevailing wind (Sefton-Nash et al., 2014). The orientation directions of the aeolian bedforms in the landing site are NW-SE and nearly E-W, indicating the NE-SW and N-S direction of prevailing winds. However, we are not able to determine the relative ages of the bedforms. In-situ observations by Zhurong rover may provide more evidence to determine the relationship between the aeolian bedforms, which will provide insights into the wind direction changes, and assessment of current and seasonal changes with the Zhurong meteorology equipment (MCS).

The sand dunes on Mars are usually dark-toned and made of mafic silicate minerals or rock fragments, e.g., Bagnold Dune Field in Gale crater (Achilles et al., 2017; Ehlmann et al., 2017). The light-toned bedforms in the study area resemble those first identified in MOC images (Thomas et al., 1999); they appear to be weathering products commonly found in the northern plains (Horgan & Bell, 2012). These light-toned bedforms may contain sulphate minerals formed from playas, or other concentrations derived from groundwater, flood, or hydrothermal activity (McCollom, 2018). An alternative explanation is that the relatively

high albedo is due to dust cover on the smooth and relatively immobile surfaces (Golombek et al., 2010). Zhurong's in-situ exploration will reveal the origin of the light-toned bedforms, and its MCS will monitor the direction and variation in the prevailing winds.

3.1.4. Polygonal Troughs

Giant polygonal troughs are pervasively distributed in Utopia Planitia and have been considered to be related to the activity of volatiles. Different origins have been proposed by previous studies (e.g., Buczkowski & Cooke, 2004; Buczkowski & McGill, 2002; Hiesinger & Head, 2000; McGill & Hills, 1992). Buczkowski et al. (2012) summarized these studies and proposed three models for the formation of giant polygons and circular graben: tectonic uplift model, drape folding model, and volumetric compaction model. Their survey of the polygons and circular graben in the Utopia Planitia supported the volumetric compaction model, and they proposed a two-stage evolution scenario for the subdued giant polygons in the southern Utopia including (a) formation of a primordial polygon due to volumetric compaction of locally thawed or never-frozen cover material and (b) partial superposition of later sedimentary deposits (Buczkowski et al., 2012). This model indicates a two-layer subsurface structure of the polygonal troughs, which could be confirmed by their detection by RoPeR onboard the Zhurong rover. Verification of this model will provide clues to the volatile evolution of the region.

3.1.5. Ridges

Various formation mechanisms have been proposed for linear or curvilinear ridges on the martian surface, including inverted fluvial channels (e.g., Burr et al., 2009; Williams et al., 2013), linear dunes (e.g., Davis et al., 2020; Ruff, 1994), lava tubes (e.g., Zhao et al., 2017), igneous dikes (e.g., Huang et al., 2012; Korteniemi et al., 2010), eskers (e.g., Banks et al., 2009; Kress & Head, 2015), or etc. The ridges in the study region are composed of rocky materials and have variable orientations, which is not consistent with a linear dune origin. The inverted channel origin is also not likely because no obvious source region and fluvial sediments are identified, and many of the ridges are straight and isolated without showing any drainage patterns. Could the ridges be formed by igneous processes (e.g., Head et al., 2006)? The Type 1 ridges are usually short and straight, and similar features have been interpreted as igneous dikes (Korteniemi et al., 2010); Type 2 ridges are longer and more sinuous, which may be similar with the ridge-like lava tubes identified in the Tharsis region (Zhao et al., 2017). In addition, an esker origin for Type 2 ridges could not be easily eliminated considering their sinuous form and the ability to cross topographic divides (Banks et al., 2009). Therefore, imaging and spectral investigations by the Zhurong rover are of critical importance to confirm the detailed morphology and rock types of the ridges to distinguish between volcanic or sedimentary/glacial origins, which can further help determine the resurfacing characteristics of the study region in the Amazonian period.

3.2. Stratigraphy and Geological Evolution

We have mapped various geomorphic features and made a geological sketch map of the 0.5-degree by 0.5-degree Zhurong landing region (Figure 4a). We propose a five-layer stratigraphic model for the mapped area (Figure 4b) based on observations and previous studies. The top layer A consists of relatively loose materials, which appear relatively smooth in high resolution visible images (Figure 2f) and show relatively low night-time temperatures at night (Figure 1c). The materials of layer A are interpreted to contain water ice and/or carbon dioxide ice, which are suggested by widely distributed pitted-wall craters (Figure 2d). Layer B beneath layer A is made of coarser and more rocky materials, identified on the basis of the rocks and boulders in the ejecta of RECs with elevated nighttime temperatures. We estimated the thickness of layer A using the diameters of RECs, assuming that the maximum depth of excavation is approximately 1/10 of the transient crater diameter, and the final crater rim-to-rim diameter for simple craters is 0.84 times the transient crater diameter (Melosh, 1989). We have identified all the RECs with available HiRISE scenes and calculated the maximum thickness at each location (Figure S3). The thickness of layer A is up to ~48 m. Layer C is composed of materials of the Vastitas Borealis Formation, which is a thin sedimentary unit with an estimated minimum average thickness of ~100 m (Head et al., 2002). Layer D is the Early Hesperian volcanic ridged plains, and its thickness is estimated to be ~800–1,000 m (Head et al., 2002). The bottom (Layer E) is the Noachian-aged basement (Frey et al., 2002).

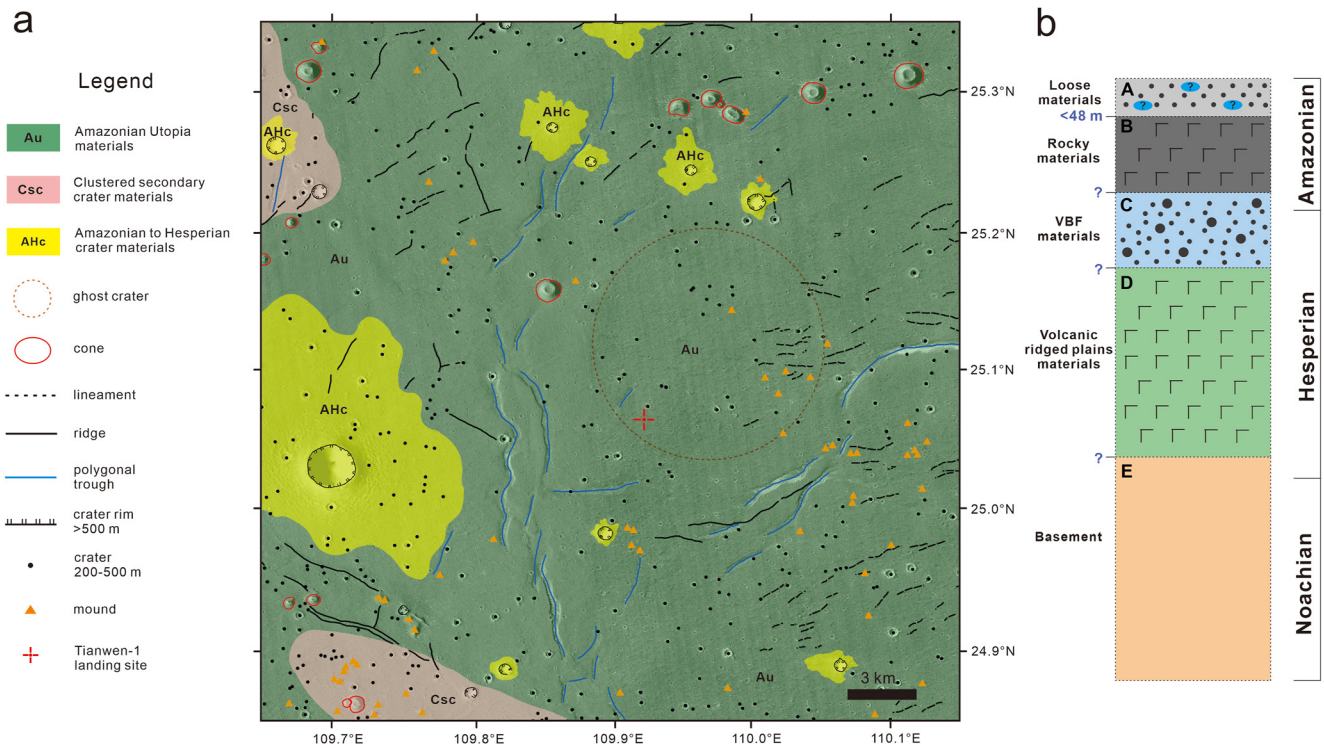

Figure 4. Geological map (a) and proposed stratigraphy (b) of the Zhurong landing region. The thickness of the layers in (b) is not to scale.

We propose a possible scenario for the geological evolution of the mapped region (Figure 4a) that can be tested and/or refined by Zhurong surface exploration and further analyses. Basaltic lava was emplaced on the underlying Noachian cratered basement during the Early Hesperian (Head et al., 2002), followed by the water/ice containing VBF materials. Amazonian lava flows or mudflows appear to have been emplaced on top of the VBF materials around ~757 Ma. Water ice and/or carbon dioxide ice are interpreted to have been deposited into the relatively loose materials due to changes in eccentricity and obliquity that altered the climatic conditions (Head et al., 2003; Laskar et al., 2002; Madeleine et al., 2009). Relatively light-toned aeolian bedforms developed and were subsequently covered by airfall dust.

4. Summary and Concluding Remarks

On the basis of our geologic mapping, we have outlined the location of key geological features and targets for exploration and further analysis in the Zhurong landing region to address these critical issues in the evolution of the northern lowlands. The questions with highest priority are: (a) Origin of pitted cones; (b) Origin of graben-like troughs; (c) Evidence for ancient oceans; (d) Evidence for mudflows; (e) Origin of surface/near surface rocks; (f) Nature of the Amazonian climate record; (g) Impact crater stratigraphy; (h) Nature/origin/age of aeolian features; and (i) Stratigraphic sequence. We have also compiled a model stratigraphic column to guide, test and refine, on the basis of ongoing and future analyses of this unique region.

Data Availability Statement

HiRISE, CTX, THEMIS, and MOLA data used in this study are available at Zenodo (https://doi.org/10.5281/zenodo.5279799). HiRISE data can also be accessed by IDs from https://www.uahirise.org/. CTX global mosaic can also be accessed from http://murray-lab.caltech.edu/CTX/index.html. MOLA and THEMIS data can also be accessed from https://ode.rsl.wustl.edu/mars/indexProductSearch.aspx. JMARS (jmars.asu.edu) was used to query and prepare data.

Acknowledgments
This study was supported by the Strategic Priority Research Program of the Chinese Academy of Sciences (XDB 41000000), the National Natural Science Foundation of China (41773061, 42002305, 41830214), the Pre-research Project on Civil Aerospace Technologies of CNSA (D020101), the Fundamental Research Funds for the Central Universities (CUGL200801, CUG2106122) and the Teaching Research Project (2020A04). We appreciate editorial handling by Editor Prof. Andrew J. Dombard. The reviews by Prof. Steven W. Ruff and an anonymous reviewer greatly improved the manuscript.

References

Achilles, C., Downs, R., Ming, D., Rampe, E., Morris, R., Treiman, A., et al. (2017). Mineralogy of an active eolian sediment from the Namib dune, Gale crater, Mars. *Journal of Geophysical Research: Planets*, *122*(11), 2344–2361. https://doi.org/10.1002/2017je005262

Banks, M. E., Lang, N. P., Kargel, J. S., McEwen, A. S., Baker, V. R., Grant, J. A., et al. (2009). An analysis of sinuous ridges in the southern Argyre Planitia, Mars using HiRISE and CTX images and MOLA data. *Journal of Geophysical Research: Planets*, *114*, E09003. https://doi.org/10.1029/2008je003244

Brož, P., & Hauber, E. (2012). A unique volcanic field in Tharsis, Mars: Pyroclastic cones as evidence for explosive eruptions. *Icarus*, *218*(1), 88–99.

Brož, P., Hauber, E., Wray, J. J., & Michael, G. (2017). Amazonian volcanism inside Valles Marineris on Mars. *Earth and Planetary Science Letters*, *473*, 122–130.

Buczkowski, D. L., & Cooke, M. L. (2004). Formation of double-ring circular grabens due to volumetric compaction over buried impact craters: Implications for thickness and nature of cover material in Utopia Planitia, Mars. *Journal of Geophysical Research: Planets*, *109*, E02006. https://doi.org/10.1029/2003je002144

Buczkowski, D. L., & McGill, G. E. (2002). Topography within circular grabens: Implications for polygon origin, Utopia Planitia, Mars. *Geophysical Research Letters*, *29*(7), 59–515954. https://doi.org/10.1029/2001gl014100

Buczkowski, D. L., Seelos, K. D., & Cooke, M. L. (2012). Giant polygons and circular graben in western Utopia basin, Mars: Exploring possible formation mechanisms. *Journal of Geophysical Research: Planets*, *117*, E08010. https://doi.org/10.1029/2011je003934

Burr, D. M., Enga, M.-T., Williams, R. M., Zimbelman, J. R., Howard, A. D., & Brennand, T. A. (2009). Pervasive aqueous paleoflow features in the Aeolis/Zephyria Plana region, Mars. *Icarus*, *200*(1), 52–76. https://doi.org/10.1016/j.icarus.2008.10.014

Christensen, P. R., Bandfield, J. L., Hamilton, V. E., Ruff, S. W., Kieffer, H. H., Titus, T. N., et al. (2001). Mars Global Surveyor Thermal Emission Spectrometer experiment: Investigation description and surface science results. *Journal of Geophysical Research: Planets*, *106*(E10), 23823–23871. https://doi.org/10.1029/2000je001370

Christensen, P. R., Jakosky, B. M., Kieffer, H. H., Malin, M. C., McSween, H. Y., Nealson, K., et al. (2004). The thermal emission imaging system (THEMIS) for the Mars 2001 Odyssey Mission. *Space Science Reviews*, *110*(1), 85–130. https://doi.org/10.1007/978-0-306-48600-5_3

Davis, J. M., Banham, S. G., Grindrod, P. M., Boazman, S. J., Balme, M. R., & Bristow, C. S. (2020). Morphology, development, and sediment dynamics of elongating linear dunes on Mars. *Geophysical Research Letters*, *47*(12), e2020GL088456. https://doi.org/10.1029/2020gl088456

Dickson, J., Kerber, L., Fassett, C., & Ehlmann, B. (2018). *A global, blended CTX mosaic of Mars with vectorized seam mapping: A new mosaicking pipeline using principles of non-destructive image editing*. Paper presented at the Lunar and planetary science conference.

Edwards, C., Nowicki, K., Christensen, P., Hill, J., Gorelick, N., & Murray, K. (2011). Mosaicking of global planetary image datasets: 1. Techniques and data processing for Thermal Emission Imaging System (THEMIS) multi-spectral data. *Journal of Geophysical Research: Planets*, *116*, E10008. https://doi.org/10.1029/2010je003755

Ehlmann, B., Edgett, K., Sutter, B., Achilles, C., Litvak, M., Lapotre, M., et al. (2017). Chemistry, mineralogy, and grain properties at Namib and High dunes, Bagnold dune field, Gale crater, Mars: A synthesis of Curiosity rover observations. *Journal of Geophysical Research: Planets*, *122*(12), 2510–2543. https://doi.org/10.1002/2017je005267

Fergason, R. L., Christensen, P. R., & Kieffer, H. H. (2006). High-resolution thermal inertia derived from the Thermal Emission Imaging System (THEMIS): Thermal model and applications. *Journal of Geophysical Research: Planets*, *111*, E12004. https://doi.org/10.1029/2006je002735

Frey, H. V., Roark, J. H., Shockey, K. M., Frey, E. L., & Sakimoto, S. E. (2002). Ancient lowlands on Mars. *Geophysical Research Letters*, *29*(10), 22–12224. https://doi.org/10.1029/2001gl013832

Golombek, M., Robinson, K., McEwen, A., Bridges, N., Ivanov, B., Tornabene, L., & Sullivan, R. (2010). Constraints on ripple migration at Meridiani Planum from Opportunity and HiRISE observations of fresh craters. *Journal of Geophysical Research: Planets*, *115*, E00F08. https://doi.org/10.1029/2010je003628

Hamilton, C. W., Fagents, S. A., & Thordarson, T. (2011). Lava–ground ice interactions in Elysium Planitia, Mars: Geomorphological and geospatial analysis of the Tartarus Colles cone groups. *Journal of Geophysical Research: Planets*, *116*, E03004. https://doi.org/10.1029/2010je003657

Head, J. W., Kreslavsky, M. A., & Pratt, S. (2002). Northern lowlands of Mars: Evidence for widespread volcanic flooding and tectonic deformation in the Hesperian Period. *Journal of Geophysical Research: Planets*, *107*(E1), 3–1329. https://doi.org/10.1029/2000je001445

Head, J. W., Mustard, J. F., Kreslavsky, M. A., Milliken, R. E., & Marchant, D. R. (2003). Recent ice ages on Mars. *Nature*, *426*(6968), 797–802. https://doi.org/10.1038/nature02114

Head, J. W., Wilson, L., Dickson, J., & Neukum, G. (2006). The Huygens-Hellas giant dike system on Mars: Implications for Late Noachian–Early Hesperian volcanic resurfacing and climatic evolution. *Geology*, *34*(4), 285–288. https://doi.org/10.1130/g22163.1

Hiesinger, H., & Head, J. W. (2000). Characteristics and origin of polygonal terrain in southern Utopia Planitia, Mars: Results from Mars Orbiter Laser Altimeter and Mars Orbiter Camera data. *Journal of Geophysical Research: Planets*, *105*(E5), 11999–12022. https://doi.org/10.1029/1999je001193

Horgan, B., & Bell, J. F., III. (2012). Widespread weathered glass on the surface of Mars. *Geology*, *40*(5), 391–394. https://doi.org/10.1130/g32755.1

Huang, J., Edwards, C. S., Horgan, B. H., Christensen, P. R., Kraft, M. D., & Xiao, L. (2012). Identification and mapping of dikes with relatively primitive compositions in Thaumasia Planum on Mars: Implications for Tharsis volcanism and the opening of Valles Marineris. *Geophysical Research Letters*, *39*, L17201. https://doi.org/10.1029/2012gl052523

Ivanov, M. A., Hiesinger, H., Erkeling, G., & Reiss, D. (2014). Mud volcanism and morphology of impact craters in Utopia Planitia on Mars: Evidence for the ancient ocean. *Icarus*, *228*, 121–140. https://doi.org/10.1016/j.icarus.2013.09.018

Jia, Y. Z., Yu, F., & Zou, Y. L. (2018). Scientific objectives and payloads of Chinese first Mars exploration. *Chinese Journal of Space Science*, *38*(5), 650–655.

Kieffer, H. H. (2013). Thermal model for analysis of Mars infrared mapping. *Journal of Geophysical Research: Planets*, *118*(3), 451–470. https://doi.org/10.1029/2012je004164

Kneissl, T., van Gasselt, S., & Neukum, G. (2011). Map-projection-independent crater size-frequency determination in GIS environments—New software tool for ArcGIS. *Planetary and Space Science*, *59*(11–12), 1243–1254. https://doi.org/10.1016/j.pss.2010.03.015

Komatsu, G., Okubo, C. H., Wray, J. J., Ojha, L., Cardinale, M., Murana, A., et al. (2016). Small edifice features in Chryse Planitia, Mars: Assessment of a mud volcano hypothesis. *Icarus*, *268*, 56–75. https://doi.org/10.1016/j.icarus.2015.12.032

Korteniemi, J., Raitala, J., Aittola, M., Ivanov, M. A., Kostama, V.-P., Öhman, T., & Hiesinger, H. (2010). Dike indicators in the Hadriaca Patera–Promethei Terra region, Mars. *Earth and Planetary Science Letters*, *294*(3–4), 466–478. https://doi.org/10.1016/j.epsl.2009.06.038

Kreslavsky, M. A., & Head, J. W. (2002). Fate of outflow channel effluents in the northern lowlands of Mars: The Vastitas Borealis Formation as a sublimation residue from frozen ponded bodies of water. *Journal of Geophysical Research: Planets*, *107*(E12), 4–1425. https://doi.org/10.1029/2001je001831

Kress, A. M., & Head, J. W. (2015). Late Noachian and early Hesperian ridge systems in the south circumpolar Dorsa Argentea Formation, Mars: Evidence for two stages of melting of an extensive late Noachian ice sheet. *Planetary and Space Science*, *109*, 1–20. https://doi.org/10.1016/j.pss.2014.11.025

Laskar, J., Levrard, B., & Mustard, J. F. (2002). Orbital forcing of the Martian polar layered deposits. *Nature*, *419*(6905), 375–377. https://doi.org/10.1038/nature01066

Madeleine, J.-B., Forget, F., Head, J. W., Levrard, B., Montmessin, F., & Millour, E. (2009). Amazonian northern mid-latitude glaciation on Mars: A proposed climate scenario. *Icarus*, *203*(2), 390–405. https://doi.org/10.1016/j.icarus.2009.04.037

Malin, M. C., Bell, J. F., Cantor, B. A., Caplinger, M. A., Calvin, W. M., Clancy, R. T., et al. (2007). Context camera investigation on board the Mars Reconnaissance Orbiter. *Journal of Geophysical Research: Planets*, *112*, E05S04. https://doi.org/10.1029/2006je002808

McCollom, T. M. (2018). Geochemical trends in the Burns formation layered sulfate deposits at Meridiani Planum, Mars, and implications for their origin. *Journal of Geophysical Research: Planets*, *123*(9), 2393–2429. https://doi.org/10.1029/2018je005718

McEwen, A. S., Eliason, E. M., Bergstrom, J. W., Bridges, N. T., Hansen, C. J., Delamere, W. A., et al. (2007). Mars reconnaissance orbiter's high resolution imaging science experiment (HiRISE). *Journal of Geophysical Research: Planets*, *112*, E05S02. https://doi.org/10.1029/2005je002605

McGill, G. E., & Hills, L. S. (1992). Origin of giant Martian polygons. *Journal of Geophysical Research: Planets*, *97*(E2), 2633–2647. https://doi.org/10.1029/91je02863

Melosh, H. J. (1989). *Impact cratering: A geologic process*. Oxford University Press.

Michael, G., & Neukum, G. (2010). Planetary surface dating from crater size–frequency distribution measurements: Partial resurfacing events and statistical age uncertainty. *Earth and Planetary Science Letters*, *294*(3–4), 223–229. https://doi.org/10.1016/j.epsl.2009.12.041

Newsom, H. E., Crumpler, L. S., Reedy, R. C., Petersen, M. T., Newsom, G. C., Evans, L. G., et al. (2007). Geochemistry of Martian soil and bedrock in mantled and less mantled terrains with gamma ray data from Mars Odyssey. *Journal of Geophysical Research*, *112*, E03S12. https://doi.org/10.1029/2006je002680

Oehler, D. Z., & Allen, C. C. (2010). Evidence for pervasive mud volcanism in Acidalia Planitia, Mars. *Icarus*, *208*(2), 636–657. https://doi.org/10.1016/j.icarus.2010.03.031

Orgel, C., Hauber, E., van Gasselt, S., Reiss, D., Johnsson, A., Ramsdale, J. D., et al. (2019). Grid mapping the northern plains of Mars: A new overview of recent water-and ice-related landforms in Acidalia Planitia. *Journal of Geophysical Research: Planets*, *124*(2), 454–482. https://doi.org/10.1029/2018je005664

Parker, T. J., Gorsline, D. S., Saunders, R. S., Pieri, D. C., & Schneeberger, D. M. (1993). Coastal geomorphology of the Martian northern plains. *Journal of Geophysical Research: Planets*, *98*(E6), 11061–11078. https://doi.org/10.1029/93je00618

Parker, T. J., Saunders, R. S., & Schneeberger, D. M. (1989). Transitional morphology in west Deuteronilus Mensae, Mars: Implications for modification of the lowland/upland boundary. *Icarus*, *82*(1), 111–145. https://doi.org/10.1016/0019-1035(89)90027-4

Pasckert, J. H., Hiesinger, H., & Reiss, D. (2012). Rheologies and ages of lava flows on Elysium Mons, Mars. *Icarus*, *219*(1), 443–457. https://doi.org/10.1016/j.icarus.2012.03.014

Presley, M. A., & Christensen, P. R. (1997). The effect of bulk density and particle size sorting on the thermal conductivity of particulate materials under Martian atmospheric pressures. *Journal of Geophysical Research: Planets*, *102*(E4), 9221–9229. https://doi.org/10.1029/97je00271

Ruff, S. (1994). *Comparison of Mars Sinous Ridges with Terrestrial Linear Dunes: Observations from the Field*. Paper presented at Lunar and Planetary Science Conference, Houston, TX.

Ruff, S. W., & Christensen, P. R. (2002). Bright and dark regions on Mars: Particle size and mineralogical characteristics based on Thermal Emission Spectrometer data. *Journal of Geophysical Research*, *107*(E12), 2–1222. https://doi.org/10.1029/2001je001580

Sefton-Nash, E., Teanby, N., Newman, C., Clancy, R., & Richardson, M. (2014). Constraints on Mars' recent equatorial wind regimes from layered deposits and comparison with general circulation model results. *Icarus*, *230*, 81–95. https://doi.org/10.1016/j.icarus.2013.11.014

Sharp, R. P. (1963). Wind ripples. *The Journal of Geology*, *71*(5), 617–636. https://doi.org/10.1086/626936

Skinner, J. A., Jr., & Tanaka, K. L. (2007). Evidence for and implications of sedimentary diapirism and mud volcanism in the southern Utopia highland–lowland boundary plain, Mars. *Icarus*, *186*(1), 41–59. https://doi.org/10.1016/j.icarus.2006.08.013

Smith, D. E., Zuber, M. T., Frey, H. V., Garvin, J. B., Head, J. W., Muhleman, D. O., et al. (2001). Mars Orbiter Laser Altimeter: Experiment summary after the first year of global mapping of Mars. *Journal of Geophysical Research*, *106*(E10), 23689–23722. https://doi.org/10.1029/2000je001364

Stockstill-Cahill, K. R., Anderson, F. S., & Hamilton, V. E. (2008). A study of low-albedo deposits within Amazonis Planitia craters: Evidence for locally derived ultramafic to mafic materials. *Journal of Geophysical Research: Planets*, *113*, E07008.

Tan, X., Liu, J., Zhang, X., Yan, W., Chen, W., Ren, X., et al. (2021). Design and validation of the scientific data products for China's Tianwen-1 mission. *Space Science Reviews*, *217*(5), 1–22. https://doi.org/10.1007/s11214-021-00843-6

Tanaka, K. L. (2005). Geology and insolation-driven climatic history of Amazonian north polar materials on Mars. *Nature*, *437*(7061), 991–994. https://doi.org/10.1038/nature04065

Tanaka, K. L., Robbins, S., Fortezzo, C., Skinner, J., Jr., & Hare, T. M. (2014). The digital global geologic map of Mars: Chronostratigraphic ages, topographic and crater morphologic characteristics, and updated resurfacing history. *Planetary and Space Science*, *95*, 11–24. https://doi.org/10.1016/j.pss.2013.03.006

Thomas, P. C., Malin, M. C., Carr, M., Danielson, G., Davies, M., Hartmann, W. K., et al. (1999). Bright dunes on Mars. *Nature*, *397*(6720), 592–594. https://doi.org/10.1038/17557

Wan, W., Wang, C., Li, C., & Wei, Y. (2020). China's first mission to Mars. *Nature Astronomy*, *4*(7), 721. https://doi.org/10.1038/s41550-020-1148-6

Williams, R. M., Irwin, R. P., III, Burr, D. M., Harrison, T., & McClelland, P. (2013). Variability in martian sinuous ridge form: Case study of Aeolis Serpens in the Aeolis Dorsa, Mars, and insight from the Mirackina paleoriver, South Australia. *Icarus*, *225*(1), 308–324. https://doi.org/10.1016/j.icarus.2013.03.016

Wu, B., Dong, J., Wang, Y., Li, Z., Chen, Z., Liu, W. C., et al. (2021). Characterization of the candidate landing region for Tianwen-1—China's First Mission to Mars. *Earth and Space Science*, *8*(6), e2021EA001670. https://doi.org/10.1029/2021ea001670

Wu, X., Liu, Y., Zhang, C., Wu, Y., Zhang, F., Du, J., et al. (2021). Geological characteristics of China's Tianwen-1 landing site at Utopia Planitia, Mars. *Icarus*, *370*(2021), 114657. https://doi.org/10.1016/j.icarus.2021.114657

Ye, P., Sun, Z., Rao, W., & Meng, L. (2017). Mission overview and key technologies of the first Mars probe of China. *Science China Technological Sciences*, *60*(5), 649–657. https://doi.org/10.1007/s11431-016-9035-5

Zhao, J., Huang, J., Kraft, M. D., Xiao, L., & Jiang, Y. (2017). Ridge-like lava tube systems in southeast Tharsis, Mars. *Geomorphology*, *295*, 831–839. https://doi.org/10.1016/j.geomorph.2017.08.023

Zimbelman, J. R. (2010). Transverse aeolian ridges on Mars: First results from HiRISE images. *Geomorphology*, *121*(1–2), 22–29. https://doi.org/10.1016/j.geomorph.2009.05.012